Unsupervised Change Detection Using Multiscale and Multiresolution Gaussian-Mixture-Model Guided by Saliency Enhancement

Dinghua Xue, Tao Lei, *Senior Member, IEEE*, Xiaohong Jia, Xingwu Wang, Tao Chen, *Member, IEEE*, and Asoke K. Nandi, *Fellow, IEEE*

***Abstract*—Popular unsupervised change detection algorithms suffer from two problems: first, the difference image generated by bitemporal images usually includes a large number of falsely changed regions due to noise corruption and illumination change; second, fuzzy clustering algorithms are sensitive to noise and they miss the relationship among feature components. To address these issues, we propose a multiscale and multiresolution Gaussian-mixture-model guided by saliency-enhancement (SE-MGMM) for change detection in bitemporal remote sensing images. The proposed SE-MGMM makes two contributions. The first is a novel salient strategy that can enhance saliency objects while suppressing the image background. The strategy uses the saliency weight information to enhance changed regions leading to the improvement of grayscale contrast between changed regions and unchanged regions. The second is that we present a Gaussian-mixture-model based on spatial multiscale and frequency multiresolution information fusion, which can effectively utilize features of difference images and improve detection results of changed regions. Experiments show that the proposed SE-MGMM is robust for both very high-resolution remote sensing images and synthetic aperture radar images. Moreover, the SE-MGMM achieves better change detection and provides better performance metrics than state-of-the-art approaches.**

***Index Terms*—Change detection, feature fusion, Gaussian-mixture-model (GMM), saliency enhancement.**

Manuscript received May 26, 2020; revised November 5, 2020, November 30, 2020, and December 12, 2020; accepted December 17, 2020. Date of publication December 23, 2020; date of current version January 21, 2021. This work was supported in part by the National Natural Science Foundation of China under Grant 61871259, Grant 61811530325 (IEC\NSFC\170396, Royal Society, U.K.), Grant 61871260, Grant 61672333, and Grant 61873155, and in part by Science and Technology Program of Shaanxi Province of China under Grant 2020NY-172. *(Corresponding author: Tao Lei.)*

Dinghua Xue and Xiaohong Jia are with the School of Electronical and Control Engineering and the Shaanxi Joint Laboratory of Artificial Intelligence, Shaanxi University of Science and Technology, Xi'an 710021, China (e-mail: xdinghua@sust.edu.cn; jiaxhsust@163.com).

Tao Lei is with the School of Electronic Information and Artificial Intelligence and the Shaanxi Joint Laboratory of Artificial Intelligence, Shaanxi University of Science and Technology, Xi'an 710021, China (e-mail: leitao@sust.edu.cn).

Xingwu Wang is with the School of Electronic Information and Artifical Intelligence, Shaanxi University of Science and Technology, Xi'an 710021, China (e-mail: wangxwu1949@163.com).

Tao Chen is with the Institute of Geophysics and Geomatics, China University of Geosciences, Wuhan 430074, China (e-mail: taochen@cug.edu.cn).

Asoke K. Nandi is with the Department of Electronic and Electrical Engineering, Brunel University London, UB8 3PH Uxbridge, U.K., and also with the School of Mechanical Engineering, Xi'an Jiaotong University, Xi'an 710049, China (e-mail: asoke.nandi@brunel.ac.uk).

Digital Object Identifier 10.1109/JSTARS.2020.3046838

I. Introduction

CHANGE detection aims to identify the changed and unchanged regions from bitemporal remote sensing images acquired over the same geographical area but at different times. Most of these changes are reflected in the location and range of ground objects, as well as the changes in their properties and states. So far, change detection techniques have attracted the attention from many researchers due to wide applications, such as urban planning and construction [1], land use [2]–[4], disaster monitoring and evaluation [5], urban environmental survey [6], acquisition of extended change information [7], etc. Currently, a lot of change detection methods have been reported to detect the changed information on this earth we live. These change detection methods can be roughly grouped into three categories: pixel-based approaches [8]–[19], object-based approaches [20]–[25], and deep learning (DL)-based approaches [26]–[34].

The pixel-based approaches include thresholding-based methods [8]–[10], clustering-based methods [11]–[15], expectation maximinzation (EM)-based methods [16]–[17], and multivariate alteration detection (MAD)-based methods [18-19]. The basic idea of thresholding is simple as it calculates the threshold of a difference image according to the grayscale distribution of pixels. By comparing the grayscale value of each pixel with the threshold, pixels are classified into two classes, i.e., changed regions and unchanged regions. Lv *et al.* [9] used a multithreshold segmentation algorithm combining with the voting strategy to optimize pixel classification. However, thresholding-based methods seriously rely on the grayscale distribution of pixels and ignore the spatial structuring information of images. Besides, they are sensitive to light and noise. To address the problems, Hao *et al.* [13] integrated local and global image information to improve change detection results of bitemporal remote sensing images. Therefore, these previous studies demonstrate that clustering-based methods outperform thresholding-based methods for change detection tasks. Furthermore, since EM can better estimate the underlying parameters with the data distribution of a difference image, Lv *et al.* [16] employed a strategy that combines multithreshold and EM attribute to improve target uniformity and obtain even better change detection results. It should also be noted that Canty and Nielsen [18] first proposed the iterative reweighted MAD (IRMAD) and Xu *et al.* [19] modeled a regularized iteratively reweighted

object-based MAD method for change detection tasks. These improved MAD methods aim to solve the limitations among current multiremote sensing image processing and promote the robustness of algorithms. Although pixel-based approaches have been widely used for different change detection tasks, this kind of methods seriously depend on the complexity of image content and image preprocessing such as registration accuracy, radiation correction, etc.

Compared to pixel-based approaches, the object-based approaches provide higher accuracy and stronger robustness than pixel-based methods, because they can effectively integrate richer features of objects for comprehensive evaluation and analysis, such as shape, texture, and spectral information of images. The object-based approaches mainly include Markov random fields (MRF)-based methods [20]–[23] and level set-based methods [24], [25]. These methods are popular for change detection tasks because they can consider the spatial relationship of neighborhood pixels. Yu *et al.* [21] first used active learning with Gaussian process to iteratively optimize the detection model, then integrated attribute (color and texture) information and contextual information into the MRF model to obtain change detection results. Touati *et al.* [22] filled the gap by proposing Bayesian and Markovian-based multimodal method. Also, Yang *et al.* [23] devoted change detection tasks using special MRF prior and variational Bayesian inference, and [23] achieved a good performance in respect of shape-preserving ability. For level set based change detection methods, Li *et al.* [24] employed edge-based level set evolution (ELSE) and region-based level set evolution to track initial change detection profiles, leading to better change detection results. Furthermore, Zhang *et al.* [25] incorporated the level set into an improved MRF model to achieve change detection of satellite images. However, object-based approaches easily suffer from the difficulty of parameter selection and excessively rely on segmentation scales.

Driven by the complex image data and wide application of change detection, many DL-based approaches [26]–[34] have been widely used for change detection tasks since they show powerful ability on feature mining. Generally, change detection concerns three types of images, i.e., synthetic aperture radar (SAR) images, VHR images, and hyperspectral images. SAR images always include one channel while VHR images usually include three channels. Compared to SAR and VHR images, hyperspectral images usually include much more channels and thus provide richer radiation, spatial, and spectral information. Therefore, it is necessary to design different networks for different change detection tasks. Liu *et al.* [26] designed a deep convolutional coupling network that achieves better change detection results than traditional approaches both on heterogeneous optical and radar images. Then, Wang *et al.* [27] applied a CNN framework for change detection problem of hyperspectral data, the framework can learn the discriminative features effectively from higher-level multisource data and enhances the generalization ability of networks. Similarly, Lei *et al.* [28] designed a symmetric Gaussian pyramid fully convolutional network, then applied it to VHR remote sensing images. The network provides excellent changed detection results due to its strong ability of feature representation. More recently, Peng *et al.* [30] presented a comprehensive summary of deep learning change detection techniques and proposed an improved UNet++ for change detection tasks to capture subtle changes in challenging scenes. In addition, in order to summarize the development and challenges of change detection, Shi *et al.* [32] presented a survey that showed there was an upward trend in the current publicly change detection datasets, but only a few of them were labeled due to the difficulty of annotation. To sum up, the DL-based approaches provide excellent change detection results due to the strong ability of feature representation. However, they have higher requirements on the quality and quantity of labeled images, but it is difficult to label the changed information in remote sensing images. Therefore, it is hard to guarantee that the DL-based approaches can be widely used for scene change detection.

For these three kinds of techniques mentioned above, they cannot be widely used for change detection tasks due to two limitations. First, change detection results based on difference images are easily affected by atmospheric environment, especially noise corruption and illumination change. Second, many unsupervised change detection methods employ fuzzy clustering to achieve the classification of changed and unchanged regions [12]–[15], but popular fuzzy clustering methods have low robustness since they are sensitive to noise and often ignore the relationship among feature components. To solve these two problems, we propose a multiscale and multiresolution Gaussian-mixture-model (GMM) guided by saliency-enhancement (SE-MGMM) for change detection in bitemporal remote sensing images. The advantages of the proposed SE-MGMM are summarized as follows.

1) The SE-MGMM uses a new saliency strategy to enhance difference images, which solves the problem that a difference image is often sensitive to noise corruption and illumination change.
2) The SE-MGMM employs a GMM based on spatial multiscale and frequency multiresolution information fusion, which solves the problem that popularly unsupervised change detection approaches insufficiently utilize the feature relationship of bitemporal images.

II. Motivations

A. Saliency Enhancement for Change Detection

Change detection is a process of comparing and analyzing changed information in bitemporal images. During this process, the quality of difference images easily influences the precision of change detection results. However, a difference image usually includes a large number of falsely changed regions due to illumination change, noise corruption, etc. And, it is difficult to distinguish falsely changed regions from the really changed regions for a difference image. Therefore, it is important to improve the quality of difference images for achieving accurate change detection.

To solve this problem, researchers have made great efforts to improve the quality of difference images [35]. In [36], Li *et al.* employed the Gabor feature extraction and variables of local similarity to enhance the contrast of difference images. Usually,

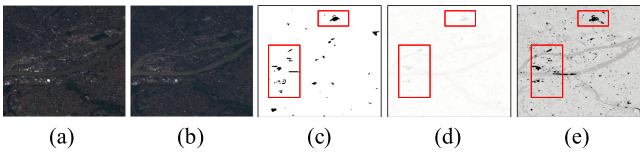

Fig. 1. "Nantes" data from Onera satellite change detection (OSCD) dataset and the enhanced difference image. (a) Pretemporal image. (b) Posttemporal image. (c) Ground truth. (d) Original difference image. (e) Difference image using saliency enhancement.

the change detection tasks obtain the change detection results by directly performing image segmentation on a difference image. Although the flowchart is very popular in many algorithms since it improves change detection results, it ignores the effect of intuitive-visual attention. In fact, the human visual system serves as a filter; it can well allocate more attention to obvious and prominent objects in images for perceptual processing. The visual system maintains vision at salient positions in an image, i.e., when we see an image, we first pay attention to salient information of the image, then use the first sight of feature information as one of our prior cognitions to analyze and understand the whole image.

Fig. 1(a) and (b) shows a pair of bitemporal images and Fig. 1(c) shows the ground truth of bitemporal images. The pair of images (582×522) were captured by the Sentinel-2 satellite in Nantes, France in 2015 and 2017, which is mainly used for geological surveys. In Fig. 1(d), it is difficult to detect changed regions due to very low contrast. It is clear that the saliency enhancement can improve the visual effect of changed regions as shown in Fig. 1(e). Therefore, it is necessary to analyze salient information of images before obtaining target areas, since salient information can guide image analysis and image processing. Driven by computer vision applications, many visual saliency models aiming to identify salient areas from images or videos have been proposed [37]–[39]. Inspired by this motivation as shown in Fig. 1, we will employ salient information of images to solve the problem that difference images are often sensitive to noise corruption and illumination change.

B. Image Information Fusion for Change Detection

For a change detection task, the early methods [8]–[10] rely on finding a good threshold to achieve binary classification, but it is difficult to find the threshold for high-dimensional data. Fuzzy c-means (FCM) is superior to thresholding methods for change detection tasks since it is unnecessary to consider the dimension of input data. Furthermore, a lot of studies show that the FCM clustering algorithm is useful for the task [12]–[15]. However, it is well known that the FCM is sensitive to noise and it ignores the spatial information of images. Thus, it is difficult to obtain good detection results if we perform the FCM directly on original difference images or saliency-enhancement images.

For the problem mentioned above, image fusion is useful due to the utilization of more and richer feature information [40]–[42]. It is a process of extracting important features of multiple original images to generate an image that contains richer information than a single image, which also has been widely

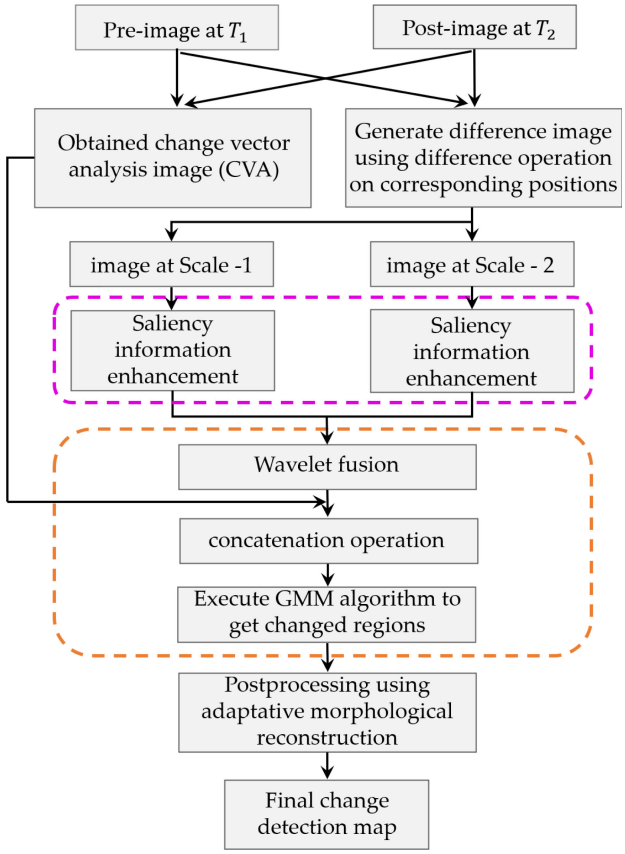

Fig. 2. Framework of SE-MGMM for change detection.

used in medical imaging, microscopic imaging, computer vision, and remote sensing [43]. The pixel-level fusion is one of the most popular image fusion methods. So far, researchers have proposed many strategies for pixel-level image fusion, such as intensity-hue-saturation (IHS) [44], [45], principal component analysis (PCA) [46], [47], multiresolution information analysis methods [14], [48], [49], etc., of which the multiresolution information analysis is more popular than other methods.

However, image fusion often causes the increase of feature dimensions. Improved FCMs show poor performance for high-dimensional images since the Euclidean distance is used for similarity measurement. The GMM is superior to the FCM since the former considers the correlation between different feature dimensions, and effectively calculates the similarity of multidimensional data using covariance. Specifically, we propose the explanations on GMM in Section III.B. Finally, we intend to utilize image fusion combining with the GMM to achieve change detection for images with complex background.

III. Methodology

In this section, we present the framework of the proposed SE-MGMM as shown in Fig. 2. It consists of the following steps.

1) Input a pair of bitemporal images and set parameters: I_1 is the preimage, I_2 is the postimage, while C is the number of mixed Gaussian distribution used for GMM and s is the scale used for multi-information fusion.

2) Generate the difference image and change vector analysis (CVA) map: There are two kinds of input images. If the input image is an optical image, then $DI = |I_2 - I_1|$; else $DI = |log(I_2) - log(I_1)|$.
3) Obtain the salient difference image: First, we use image down-sampling to generate a multiscale difference image, then calculate the weight of each saliency cue, separately. By combining advantages of various saliency cues, we obtain a multiscale saliency image.
4) Implement image segmentation: We first perform wavelet fusion on saliency-guided difference images. In addition, we add a CVA channel to the fused image to utilize much more image information. Finally, the GMM algorithm is executed to achieve change detection.
5) Implement postprocessing: Image postprocessing is helpful for improving change detection results. We use adaptive morphological reconstruction to narrow the difference between experimental results and the ground truth.
6) Output the change detection result.

A. Saliency Enhancement

In computer vision tasks, salient information is often used to highlight interesting objects while suppressing background in an image [50]. In practical applications, saliency detection can guide image co-segmentation. In this article, we first perform standard *k*-means algorithm on the original difference image to obtain fake labels, and then calculate the saliency weight using obtained fake labels.

Three cues are used to calculate saliency weights here: the contrast cue is mainly used to represent the similarity of attributes between objects and backgrounds in an image, such as intensity, color, shape and other attributes. Contrast-based methods [51], [52] focus on calculating global saliency information of an image, and they are very popular for saliency measurement. The contrast cue w^c is often defined as follows:

$$w^c(C) = \sum_{i=1, i\neq C}^{C} \left(\frac{N_{k^i}}{N_I} \left\| k^C - k^i \right\|_2 \right) \tag{1}$$

where C is the number of clusters for the *k*-means algorithm, k^i represents center value of the *i*th cluster, N_I represents the number of pixels of the input image, and N_{k^i} represents the number of pixels of the *i*th clusters. $\frac{N_{k^i}}{N_I}$ mainly assigns the weight to each pixel that belongs to the *i*th class. The Euclidean distance is used to measure the similarity between pixels in *C*th cluster and other clusters in (1).

Although cues described above can obtain better salient information for images, they are insufficient for remote sensing images with complex background and low contrast. As spatial relationship of objects in images plays a vital role for human visual attention mechanism [53], it is also employed for saliency measurement. The description of salient information based on spatial relationships is presented as follows:

$$w^s(C) = \frac{1}{N_{k^C}} \sum_{j=1}^{N_I} \left[\|A_j - A_o\|^2 \times \delta(L(A_j) - L(k^C)) \right] \tag{2}$$

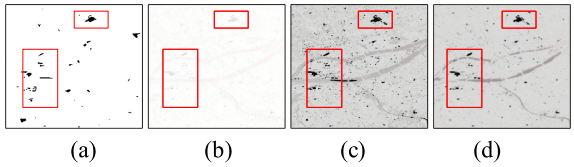

Fig. 3. Comparison of difference images using saliency weight cues. (a) Ground truth, (b) original difference image, (c) saliency-guided difference image using w^c and w^s, and (d) saliency-guided difference image using w^c, w^s, and w^m.

where the N_{k^C} represents the number of pixels in the *C*th cluster, the A_j represents the coordinate of the *j*th pixel in the image, and the A_o represents the coordinate of the center pixel of an image. The $L(A_j)$ is used to achieve the mapping operation from the pixel A_j to its class label. The value of $\delta(\Omega)$ is either 0 or 1. If Ω is 0, then the value of $\delta(\Omega)$ equals 1; otherwise, the value of $\delta(\Omega)$ equals 0. Although the w^s is useful for saliency detection when objects are closely located in the center of the image, it is difficult to apply (2) directly to change detection tasks since many small changed regions are randomly distributed in different positions of the image.

In view of this problem, we define a new salient information cue (w^m) that reduces the relevant information of changed and unchanged regions by using both local and global spatial information. The $w^m(C)$ is defined as follows:

$$w^m(C) = \frac{1}{N_{k^C}} \sum_{j=1}^{N_I} \left[\|A_j - k_m\|^2 \times \delta(L(A_j) - L(k^C)) \right] \tag{3}$$

where k_m represents the largest cluster center in the fake label. Then, we normalize each weight cue, and further design a new salient information cue ($W(C)$) that fuses three popular saliency weights

$$W(C) = w^c(C) \times w^s(C) \times w^m(C) \tag{4}$$

$$W(C) \rightarrow S(\cdot) \tag{5}$$

where $W(C)$ denotes the final saliency weight cue of pixels belonging to *C*th class. It can be seen from (1) to (4) that if the value of $W(C)$ is larger, then the similarity between the *C*th class and really changed regions will be higher. $S(\cdot)$ denotes the mapping information of saliency weight in the image.

To demonstrate the effectiveness of the proposed saliency cue, Fig. 3 shows the comparison of difference images using saliency-guided weight cues. Fig. 3(b) shows a low contrast image. However, Fig. 3(c) and (d) shows strong contrast between the changed and unchanged regions. It is clear that Fig. 3 demonstrates that the saliency information improves the quality of the difference image, and Fig. 3(c) and (d) shows that w^m reduces the relevant information and similarity of changed and unchanged regions. By comparing Figs. 1 and 3, we can see that the strategy of saliency enhancement is helpful for improving the quality of difference images.

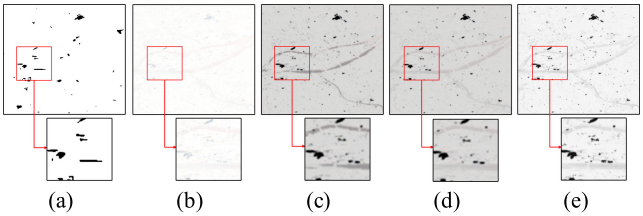

Fig. 4. Comparison of image fusion effect using SM-FM strategy. (a) Ground truth, (b) original difference image, (c) scale-1 saliency difference image, (d) scale-2 saliency difference image, and (e) SM-FM image.

B. GMM Based on SM-FM

The main factors deciding change detection results involve difference feature extraction and classification algorithms. In Section III-A, the saliency weight cue is employed to obtain better difference images, which is helpful for improving difference feature extraction. Furthermore, both information fusion and wavelet transform (WT) are also popular strategies [42] aiming to obtain richer image features, which is significant for improving the change detection accuracy of bitemporal images.

It is well known that multiscale information fusion can obtain richer image spatial features [40], [41] while WT can obtain better image frequency features. For image fusion based on multiscale information, down-sampling is often performed to obtain multiscale images. By combining these images with different scales, richer spatial features will be exploited. For image fusion based on WT, it is more effective to combine important perceptual features of images due to shift invariance of WT. Moreover, the WT possesses good localization and multiresolution characteristic, which provides horizontal, vertical, diagonal information as well as low- and high-pass components. In this article, we present an image fusion strategy that utilizes both spatial multiscale and frequency multiresolution (SM-FM). First, we use down-sampling operation to obtain multiscale difference images I_{s_1} and I_{s_2}, then perform saliency enhancement to obtain improved difference images $O_{s_1(\cdot)}$ and $O_{s_2(\cdot)}$. Second, we perform wavelet transform fusion on O_1 and O_2. Finally, the fused image is given as follows:

$$O = w_{dwt}^{-1}(\rho(w_{dwt}(O_{s_1(\cdot)}), w_{dwt}(O_{s_2(\cdot)}))) \tag{6}$$

where w_{dwt} and w_{dwt}^{-1} denote the wavelet transform and the inverse wavelet transform, respectively, O is the final fusion image, and $\rho(\cdot)$ denotes the implementation of maximum fusion rule.

To demonstrate the effectiveness of the proposed SM-FM, we apply the SM-FM to Nantes data, and Fig. 4 shows the comparison of image fusion results using SM-FM strategy. We can see that the WT maintains important feature information while suppressing noise information, and the multiscale operator effectively suppresses image background information. At the same time, it can be seen from Fig. 4(e) that the fusion operation further suppresses noise, and thus, the SM-FM shows better local detection ability due to the employment of richer image features.

In practice, CVA is very useful for change detection tasks, and it is usually integrated into fused images to improve the detection accuracy. As mentioned above, the pros and cons of classification algorithms are another important factor that affects the final change detection results. Most studies employ FCM to achieve a binary classification, i.e., changed and unchanged regions. However, FCM utilizes the Euclidean distance to achieve similarity measurement, which ignores the relationship between different feature components. Here, we consider GMM as the classification algorithm to achieve change detection tasks. On the one hand, GMM considers the prior probability of pixel distribution, which is helpful for obtaining better post-probability distribution. On the other hand, GMM employs the covariance matrix to obtain the relationship between different feature components. Therefore, GMM often shows better performance for data with complex distribution.

The probability density function of GMM is expressed as the weighted sum of C Gaussian component densities, which is specifically defined as follows:

$$p(O) = \sum_{i=1}^{C} \pi_i p(O|\mu_i, \Sigma_i) \tag{7}$$

where C denotes the number of mixed Gaussian distributions, O denotes a vector of continuous dimension data, μ_i denotes the mean value of the ith Gaussian component, Σ_i is the covariance matrix of the ith Gaussian component, π_i is the prior probability of each component, $\pi_i \geq 0$, and $\sum_{i=1}^{C} \pi_i = 1$. The density of each component is determined by the variable Gaussian function defined as follows:

$$p(O|\mu_i, \Sigma_i) = \frac{1}{(2\pi)^{\frac{D}{2}}(\Sigma_i)^{\frac{1}{2}}} exp\left\{-\frac{1}{2}(O-\mu_i)^T \Sigma_i^{-1}(O-\mu_i)\right\} \tag{8}$$

where D denotes the dimensionality of an image and T denotes transpose operation. By performing the expectation maximization iteratively until the largest probability value is obtained on the probability density function, we can obtain related parameters of GMM as follows:

$$u_{in} = \frac{\pi_i p(O_n|\mu_i, \Sigma_i)}{\sum_{i=1}^{C} \pi_i p(O_n|\mu_i, \Sigma_i)} \tag{9}$$

$$\mu_i = \frac{\sum_{n=1}^{N} u_{in} O_n}{\sum_{n=1}^{N} u_{in}} \tag{10}$$

$$\Sigma_i = \frac{\sum_{n=1}^{N} u_{in}(O_n - \mu_i)^T (O_n - \mu_i)}{\sum_{n=1}^{N} u_{in}} \tag{11}$$

$$\pi_i = \frac{1}{N} \sum_{n=1}^{N} u_{in} \tag{12}$$

where N denotes the number of pixels in an image, u_{in} denotes the posterior probability.

Based on the above analysis, we propose a multiscale information fusion method combined with GMM to achieve change detection. Fig. 5 shows the comparison of image segmentation results using different strategies. It is clear that both the image fusion strategy and GMM are helpful for improving change detection results.

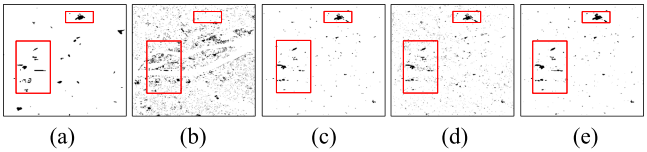

Fig. 5. Comparison of image segmentation results using different strategies. (a) Ground truth, (b) difference image + FCM, (c) SM-FM image + FCM, (d) difference image + GMM, and (e) SM-FM image + GMM.

C. Postprocessing for Change Detection

Generally, the goal of change detection is to obtain a binary image in which the foreground denotes changed regions and the background denotes unchanged regions. Based on Sections III-A and III-B, we can obtain a binary image by utilizing the proposed model on a pair of bitemporal images. However, the bitemporal images often include a lot of small and isolated regions since remote sensing images have complex background information. In practical applications, as morphological filtering is one of the most popular methods for the removal of small objects in images [48], it is usually employed to remove those isolated regions that are considered as falsely changed regions.

Despite the fact that the classic morphological opening or closing operations can effectively improve binary segmentation results, they often smooth boundaries of main objects as well. Removing false objects while maintaining details of real objects are usually difficult for morphological filters. For this problem, morphological reconstruction is an excellent tool, and it has been widely used for object detection [54], [55]. It is able to achieve binary image filtering while maintaining large objects unchanged. Here, we employ morphological reconstructions to optimize the output result from GMM. R^c denotes morphological closing reconstructions, and is defined as follows:

$$R^c(f, B) = R^{\varepsilon}(R^{\delta}(f, B), B) \tag{13}$$

where R^{ε} and R^{δ} denote morphological erosion and dilation reconstruction, respectively, f denotes a binary output from GMM, and B is a structuring element. If the size of B is too large, some real objects will be removed. On the contrary, some false objects will be maintained when the size of B is too small. Therefore, the operation requires to set the suitable size of B to control image reconstruction results. To address the issue, we propose an adaptive morphological reconstruction for change detection. For example, a small B can be selected when changed regions are small, and a large B should be selected when changed regions are large. For the adaptive morphological reconstruction, we first compute the ratio of connected components in an image. If the ratio is large, then we choose a large B, vice versa. In this article, the parameter used for B is computed as follows:

$$r = 10 \times round\left(\frac{S}{M \times N}\right) + 1 \tag{14}$$

where S denotes the region of connected components in an image, M and N denote the width and height of the image, respectively. The change detection results are shown in Fig. 6, and it is clear that the postprocessing can improve change detection results by removing many falsely detected small regions.

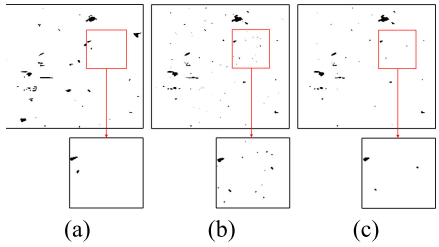

Fig. 6. Comparison of change detection results. (a) Ground truth, (b) SM-FM image + GMM, and (c) postprocessing on (b).

Algorithm 1: Multiscale and Multiresolution Gaussian-Mixture-Model Guided by Saliency Enhancement (SE-MGMM).

Input: I_1 (a pretemporal image), I_2 (a posttemporal image)
Initialize: set the values to C (the number of mixed Gaussian distribution) and s (the scale parameter used for multi-information fusion)
Compute DI, CVA
If I_1 is optical image **then**
  $DI = |I_2 - I_1|$
Else
  $DI = |log(I_2) - log(I_1)|$
End if
$CVA(i,j) = (\sum_{n=1}^{N} [I_2(i,j,n) - I_1(i,j,n)]^2)^{(\frac{1}{2})}$, N denotes the dimension of input images
Compute I_{s_1}, I_{s_2}
$I_{s_1} = DI$, $I_{s_2} = down - sampling(DI)$
Compute w^c, w^s and w^m on I_{s_1}, I_{s_2}, by implementing (1) to (3)
$W(C) = w^c(C) \times w^s(C) \times w^m(C)$
$O = w_{dwt}^{-1}(p(w_{dwt}(O_{s_1(\cdot)}), w_{dwt}(O_{s_1(\cdot)}))$
$O = (O : CVA)$
Execute GMM algorithm on O for obtaining f
$r = 10 \times round(S/(M \times N)) + 1$
Output: I_o (a binary image), $I_o = R^c(f, B)$

Based on the analysis above, we present the algorithm description of the SE-MGMM as shown in Algorithm 1.

IV. Experiments

To demonstrate the superiority of the proposed SE-MGMM, several popular approaches, i.e., change detection based principal component analysis and *k*-means (PCA-Kmeans) [11], change detection based on a robust semisupervised FCM (Semi-FCM) [12], change detection based on fuzzy clustering method and Markov random field (MRFFCM) [20], change detection using iteratively reweighted object-based MAD method (IRO-MAD) [19], change detection using fast fuzzy c-means clustering (CDFFCM) [14], change detection based on convolutional-wavelet neural networks (CWNNs) [56] and change detection using pixel pairwise-based Markov random field model (PP-MRF) [22] are considered as comparative approaches in this article.

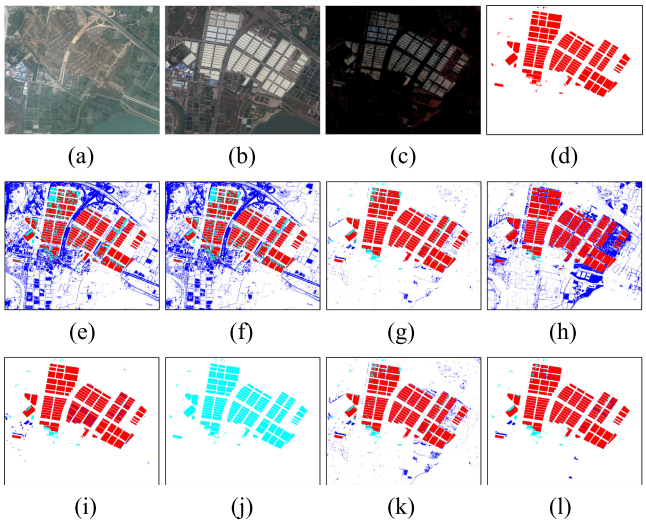

Fig. 7. Experimental results on the first group of data (mainly including building changes). (a) Pretemporal image. (b) Posttemporal image. (c) Difference image. (d) Ground truth. (e) PCA-Kmeans. (f) Semi-FCM. (g) MRFFCM. (h) IRO-MAD. (i) CDFFCM. (j) CWNN. (k) PP-MRF. (l) SE-MGMM. Note that the red color denotes truly changed regions, the blue color denotes falsely detected regions, and the cyan color denotes truly missed regions.

In our experiments, the parameter setting of comparative approaches follows original papers. We set $C = 5$ and $s = 2$ for the SE-MGMM. All approaches are implemented on a DELL desktop with Intel(R) Core (TM) CPU, i7-8700, 3.20 GHz, 64 GB RAM.

A. Dataset Description

In our experiments, six groups of images are considered as testing data to verify the effectiveness and robustness of the proposed SE-MGMM, where each group of images include a pretemporal image, a posttemporal image, and a ground truth image. To avoid the influence on bitemporal images acquired by different remote sensing sensors, typical corrections, such as image coregistration and relative radiometric correction, were done on these images.

The first group of data (from 2020-Google dataset) [57] as shown in Fig. 7(a)–(c) mainly reflect building changes. The VHR bitemporal images (4872 × 4024) with a spatial resolution of 0.55 m were acquired between 2006 and 2019 at the suburb areas of Guangzhou City, China.

The second group of data (from 2020-LEVIR dataset) [58] mainly include land changes and construction growth. The VHR bitemporal images (1024 × 1024) as shown in Fig. 8(a)–(c) were acquired with a time span of 5 to 14 years; the spatial resolution is 0.5 m.

The third group of data from[1] [59] are as shown in Fig. 9(a)–(c). Their changed regions mainly consist of new buildings and the image size is 650 × 650.

The fourth group of data were obtained by the Earth Observation Satellite 5 (SPOT5) at Tianjin, China, in April 2008 and February 2009. The bitemporal images generated by fusing

[1][Online]. Available: https://github.com/hbaudhuin/LamboiseNet

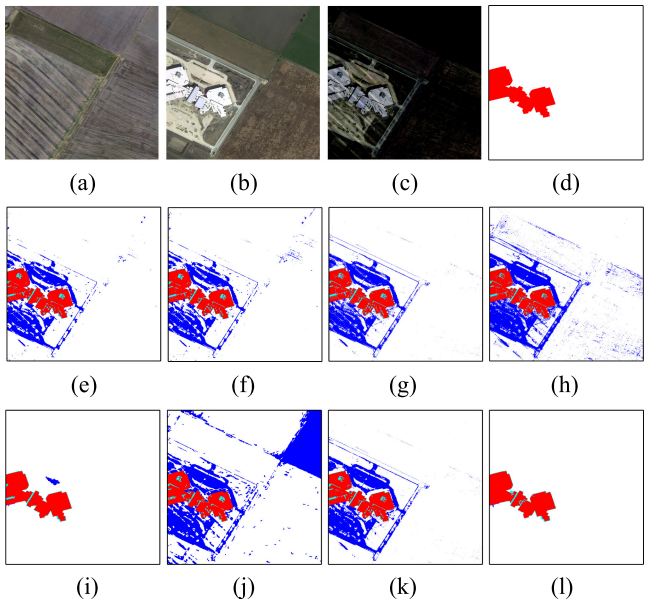

Fig. 8. Experimental results on the second group of data (mainly including land changes and construction growth). (a) Pretemporal image. (b) Posttemporal image. (c) Difference image. (d) Ground truth. (e) PCA-Kmeans. (f) Semi-FCM. (g) MRFFCM. (h) IRO-MAD. (i) CDFFCM. (j) CWNN. (k) PP-MRF. (l) SE-MGMM. Note that the red color denotes truly changed regions, the blue color denotes falsely detected regions, and the cyan color denotes truly missed regions.

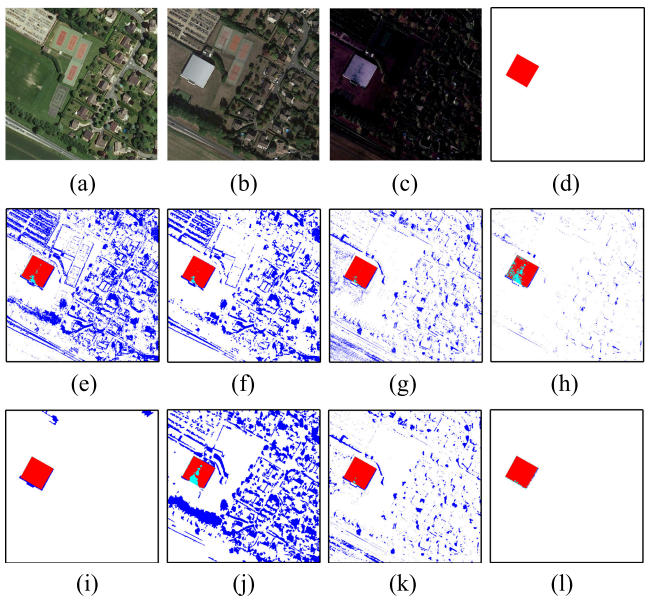

Fig. 9. Experimental results on the third group of data (mainly including new buildings change). (a) Pretemporal image. (b) Posttemporal image. (c) Difference image. (d) Ground truth. (e) PCA-Kmeans. (f) Semi-FCM. (g) MRFFCM. (h) IRO-MAD. (i) CDFFCM. (j) CWNN. (k) PP-MRF. (l) SE-MGMM. Note that the red color denotes truly changed regions, the blue color denotes falsely detected regions, and the cyan color denotes truly missed regions.

panchromatic band and multispectral bands have image size of 600 × 600 and spatial resolution of 2.5 m. This group of data covers farmland, roads, and buildings as shown in Fig. 10(a)–(c).

The fifth group of data were captured by the Sentinel-2 at the capital city of Abu Dhabi in 2015 and 2018, the images with size of 515 × 468 are shown in Fig. 11(a)–(c). The changed regions include new buildings or new roads during the two periods.

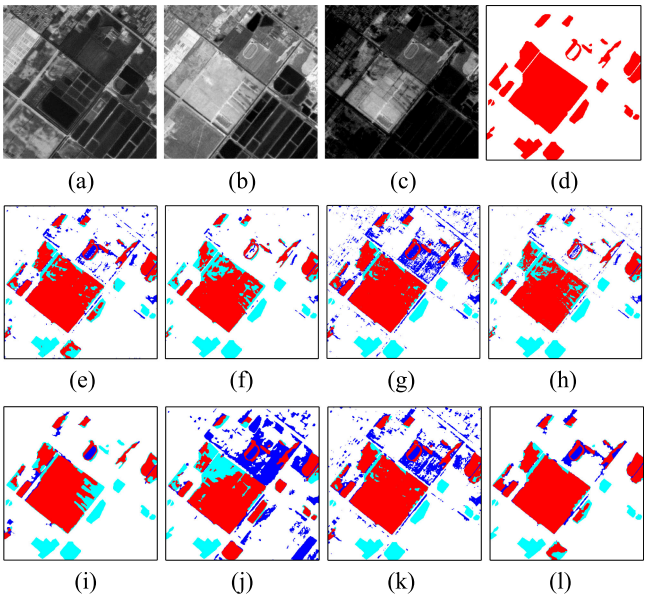

Fig. 10. Experimental results on the fourth group of data (mainly including farmland, roads, and building changes). (a) Pretemporal image. (b) Posttemporal image. (c) Difference image. (d) Ground truth. (e) PCA-Kmeans. (f) Semi-FCM. (g) MRFFCM. (h) IRO-MAD. (i) CDFFCM. (j) CWNN. (k) PP-MRF. (l) SE-MGMM. Note that the red color denotes truly changed regions, the blue color denotes falsely detected regions, and the cyan color denotes truly missed regions.

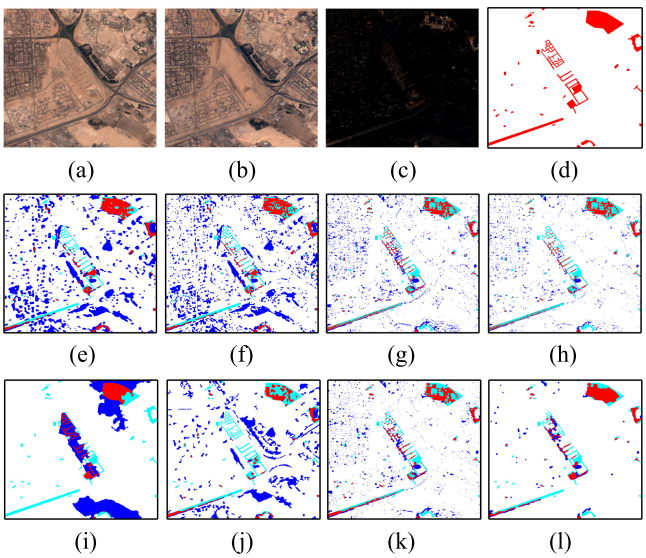

Fig. 11. Experimental results on the fifth group of data (mainly including new buildings and roads changes). (a) Pretemporal image. (b) Posttemporal image. (c) Difference image. (d) Ground truth. (e) PCA-Kmeans. (f) Semi-FCM. (g) MRFFCM. (h) IRO-MAD. (i) CDFFCM. (j) CWNN. (k) PP-MRF. (l) SE-MGMM. Note that the red color denotes truly changed regions, the blue color denotes falsely detected regions, and the cyan color denotes truly missed regions.

The final group of data were obtained by the Radarsat-2 sensor at the Yellow River basin in China. The bitemporal images with size of 280 × 450 were taken during the summer floods in June 2008 and June 2009. The changed regions mainly include water and land as shown in Fig. 12(a)–(c).

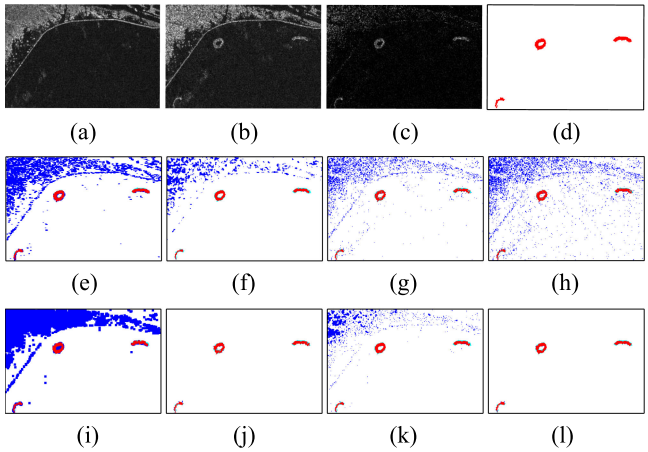

Fig. 12. Experimental results on the sixth group of data (mainly including water and land changes). (a) Pretemporal image. (b) Posttemporal image. (c) Difference image. (d) Ground truth. (e) PCA-Kmeans. (f) Semi-FCM. (g) MRF-FCM. (h) IRO-MAD. (i) CDFFCM. (j) CWNN. (k) PP-MRF. (l) SE-MGMM. Note that the red color denotes truly changed regions, the blue color denotes falsely detected regions, and the cyan color denotes truly missed regions.

B. Evaluation Indices

Four popular indices including OE (Overall error), CA (Correct accuracy of classification), KP (Kappa) and $F1\text{-}score$, are often used for the evaluation of change detection methods. Here we present the definition of these four indices. The $F1\text{-}score$ is an important index for object detection and it is defined as

$$F1 - score = \frac{2 \times Pre \times Re}{Pre + Re} \tag{15}$$

where the $Precision$ (Pre) denotes the ratio of detected areas that are really changed regions in totally detected regions. The $Recall$ (Re) denotes the ratio of detected areas that are really changed regions compare to ground truths, i.e., $Pre = \frac{TP}{(TP+FP)}$ and $Re = \frac{TP}{(TP+FN)}$. For the Pre and Re, the FP (false positive) denotes the total pixels over-detected, the FN (false negative) denotes total pixels miss-detected, the TN (true negative) denotes total pixels accurate-detected on really unchanged regions, and the TP (true positive) denotes total pixels accurate-detected on really changed regions, respectively. Generally, a large value of $F1\text{-}score$ means that the result is good while a small value means that the algorithm is inefficient for the test data.

The OE is usually used to evaluate the overall error ratio of object detection, and it is defined as

$$OE = \frac{FP + FN}{TP + TN + FP + FN}. \tag{16}$$

In general, a small value of OE corresponds to a good change detection result due to low error ratio. The KP is often used for the evaluation of unsupervised image segmentation, and it is defined as

$$KP = \frac{CA - P}{1 - P} \tag{17}$$

TABLE I
QUANTITATIVE EVALUATION RESULTS ON THE FIRST GROUP OF DATA, THE BEST VALUES ARE IN BOLD

Method	Evaluation Indices			
	OE	CA	KP	$F1\text{-}score$
PCA-Kmeans [11]	0.2416	0.7584	0.3748	0.5086
Semi-FCM [12]	0.2181	0.7819	0.4034	0.5271
MRFFCM [20]	0.0348	0.9652	0.8692	0.8898
IRO-MAD [19]	0.1320	0.8680	0.6232	0.6993
CDFFCM [14]	0.0228	0.9772	0.9156	0.9293
CWNN [56]	-	-	-	-
PP-MRF [22]	0.0384	0.9616	0.8599	0.8828
SE-MGMM	**0.0180**	**0.9820**	**0.9319**	**0.9426**

TABLE II
QUANTITATIVE EVALUATION RESULTS ON THE SECOND GROUP OF DATA, THE BEST VALUES ARE IN BOLD

Method	Evaluation Indices			
	OE	CA	KP	$F1\text{-}score$
PCA-Kmeans [11]	0.0948	0.9052	0.5040	0.5483
Semi-FCM [12]	0.0941	0.9059	0.5022	0.5465
MRFFCM [20]	0.1051	0.8949	0.4635	0.5121
IRO-MAD [19]	0.1456	0.8544	0.3796	0.4396
CDFFCM [14]	0.0077	0.9923	0.9356	0.9397
CWNN [56]	0.2114	0.7856	0.2742	0.3496
PP-MRF [22]	0.1123	0.8877	0.4541	0.5045
SE-MGMM	**0.0049**	**0.9951**	**0.9581**	**0.9607**

TABLE III
QUANTITATIVE EVALUATION RESULTS ON THE THIRD GROUP OF DATA, THE BEST VALUES ARE IN BOLD

Method	Evaluation Indices			
	OE	CA	KP	$F1\text{-}score$
PCA-Kmeans [11]	0.2477	0.7523	0.1210	0.1626
Semi-FCM [12]	0.1874	0.8126	0.1722	0.2104
MRFFCM [20]	0.0861	0.9139	0.3400	0.3677
IRO-MAD [19]	0.0206	0.9794	0.6421	0.6525
CDFFCM [14]	0.0068	0.9932	0.8798	0.8833
CWNN [56]	0.2725	0.7275	0.0950	0.1381
PP-MRF [22]	0.0688	0.9312	0.4006	0.4249
SE-MGMM	**0.0014**	**0.9986**	**0.9728**	**0.9734**

where CA and P can be computed, respectively

$$CA = \frac{TP + TN}{TP + TN + FP + FN} \tag{18}$$

$$P = \frac{\begin{bmatrix}(TP + FP) \times (TP + FN) \times \\ (FN + TN) \times (FP + TN)\end{bmatrix}}{(TP + TN + FP + FN)^2}. \tag{19}$$

C. Experiments

We applied different comparative approaches and the proposed SE-MGMM on six groups of bitemporal images. Figs. 7–12 show detected results on changed regions. Here, the regions marked by red color denote truly changed regions, the regions marked by blue color denote false-detected regions, and the regions marked by cyan color denote truly missed regions.

Fig. 7(a) and (b) shows the suburb areas in difference periods, these changes mainly focus on building changes. Fig. 7(e) and (f) suffers from a serious problem that the change detection results contain too many falsely changed regions due to the background of the difference image includes complex information as shown in Fig. 7(c). Clearly, IRO-MAD provides a higher value of $F1\text{-}score$ than PCA-Kmeans and Semi-FCM, since it can detect the changes of unstable points in bitemporal images. Thus, it detected fewer falsely changed regions (blue) than the first two comparative methods as shown in Fig. 7(e) and (f). Apparently, Fig. 7(g), (i), and (k) shows better visual effects and higher values of $F1\text{-}score$ since both MRFFCM and PP-MRF utilize MRF to characterize the relationship between neighboring pixels. Moreover, CDFFCM focuses on structural information leading to a better change detection result. In fact, CWNN fails to process the bitemporal images due to memory overflow. By contrast, the proposed SE-MGMM provides the largest value of $F1\text{-}score$ and the smallest value of OE as shown in Table I since it adopts saliency-enhancement to suppress falsely changed regions and uses MGMM instead of FCM to obtain better image segmentation results.

From Fig. 8(a)–(d), it can be seen that the visual effect of the difference image includes some falsely changed information since the ground information changes over time. All testing approaches can generate changed regions, but PCA-Kmeans, Semi-FCM, MRFFCM, IRO-MAD, CWNN, and PP-MRF suffer from the over detection problem as shown in Fig. 8(e), (h), (j), and (k). However, Fig. 8(i) shows better result than other comparative methods since it effectively exploits the image structural information by performing image segmentation on pre- and posttemporal images, respectively. Compared to Fig. 8(i), Fig. 8(l) is closer to the ground truth image and includes fewer falsely detected regions (blue) and truly missed regions (cyan), which shows that saliency enhancement is helpful for suppressing background information and enhancing foreground objects. Consequently, the SE-MGMM provides the largest value of KP and $F1\text{-}score$ as shown in Table II, which further shows the advantages of the proposed SE-MGMM for change detection.

The changed areas in third group of bitemporal images is very clear as shown in Fig. 9(a) and (b). Therefore, all comparative methods can acquire good change detection results. Similar to the first two group of bitemporal images, the third group of data also include complex background as shown in Fig. 9(c). Fig. 9(e), (f), and (j) include more falsely changed background objects, which shows that PCA-Kmeans, Semi-FCM, and MRFFCM fail to detect changed information for the third group of data. We can see that both MRFFCM and PP-MRF detected fewer falsely changed areas, which demonstrates MRF-based methods are valid for this type of data. Also, it should be noted that IRO-MAD and CDFFCM perform a better background suppression

TABLE IV
QUANTITATIVE EVALUATION RESULTS ON THE FOURTH GROUP OF DATA, THE BEST VALUES ARE IN BOLD

Method	Evaluation Indices			
	OE	CA	KP	$F1$-$score$
PCA-Kmeans [11]	0.1047	0.8953	0.7176	0.7867
Semi-FCM [12]	0.1317	0.8682	0.6328	0.7111
MRFFCM [20]	0.1604	0.8396	0.6060	0.7181
IRO-MAD [19]	0.1100	0.8900	0.6839	0.7521
CDFFCM [14]	0.1222	0.8778	0.6651	0.7401
CWNN [56]	0.2193	0.7807	0.4720	0.6241
PP-MRF [22]	0.1553	0.8447	0.6092	0.7156
SE-MGMM	**0.0829**	**0.9171**	**0.7770**	**0.8318**

TABLE V
QUANTITATIVE EVALUATION RESULTS ON THE FIFTH GROUP OF DATA, THE BEST VALUES ARE IN BOLD

Method	Evaluation Indices			
	OE	CA	KP	$F1$-$score$
PCA-Kmeans [11]	0.1720	0.8280	0.2258	0.2991
Semi-FCM [12]	0.1713	0.8287	0.2058	0.2801
MRFFCM [20]	0.0859	0.9141	0.3657	0.4113
IRO-MAD [19]	0.0693	0.9307	0.3790	0.4156
CDFFCM [14]	0.1406	0.8594	0.2229	0.3122
CWNN [56]	0.1364	0.8636	0.1721	0.2403
PP-MRF [22]	0.0706	0.9294	0.4273	0.4650
SE-MGMM	**0.0467**	**0.9533**	**0.5868**	**0.6115**

TABLE VI
QUANTITATIVE EVALUATION RESULTS ON THE SIXTH GROUP OF DATA, THE BEST VALUES ARE IN BOLD

Method	Evaluation Indices			
	OE	CA	KP	$F1$-$score$
PCA-Kmeans [11]	0.1492	0.8508	0.0969	0.1147
Semi-FCM [12]	0.0543	0.9457	0.2123	0.2265
MRFFCM [20]	0.0583	0.9417	0.2034	0.2179
IRO-MAD [19]	0.0826	0.9174	0.1622	0.1781
CDFFCM [14]	0.7748	0.2252	0.0022	0.3612
CWNN [56]	0.0243	0.9757	0.8376	0.8506
PP-MRF [22]	0.0380	0.9620	0.2954	0.3075
SE-MGMM	**0.0023**	**0.9977**	**0.8807**	**0.8818**

effect as shown in Fig. 9(h) and (i). Furthermore, the proposed SE-MGMM outperforms comparative methods in visual effect and it obtains an extra 9% than the best result from comparative approaches on $F1$-$score$ as shown in Table III.

Fig. 10(a) and (b) shows the fourth group of data. The changes in the bitemporal images mainly include farmlands, roads, and buildings. In Fig. 10, all testing approaches can generate changed regions, but the MRFFCM, CWNN, and PP-MRF include a lot of falsely changed regions as shown in Fig. 10(g), (j), and (k). In contrast, Fig. 10(f) and (h) suffers from a serious problem of leak detection since Semi-FCM is a postclassification approach. From Fig. 10(h) and Table IV, we can see that IRO-MAD provides a larger value of $F1$-$score$ than Semi-FCM, MRFFCM, CWNN, and PP-MRF. Among the comparative methods, both PCA-Kmeans and CDFFCM provide better results as shown Fig. 10(e) and (i). Finally, as can be seen from Fig. 10(l), SE-MGMM shows a better detection result as it adopts saliency-enhancement to suppress falsely changed regions. Table IV shows advantages of the SE-MGMM on the fourth group of data.

The experimental results on the fifth group of data are shown in Fig. 11, they are complex and show low contrast of intensity and hue as shown in Fig. 11 (a) and (b). Therefore, the original difference image also shows low contrast between changed regions and unchanged regions as shown in Fig. 11(c), which easily leads to poor results for change detection. PCA-Kmeans, Semi-FCM, CDFFCM, and CWNN show poor results that include many falsely detected regions as shown in Fig. 11(e), (f), (i), and (j), i.e., blue regions. It is observed that these comparative approaches are sensitive to the quality of difference images. However, Fig. 11(g), (h), and (k) shows better visual effect, which demonstrates that the MRFFCM, IRO-MAD, and PP-MRF are available for this kind of images. Moreover, the SE-MGMM provides the best detection result that includes fewer falsely changed regions and more truly changed regions as shown in Fig. 11(l), which further demonstrates that the strategy is useful for suppressing background and enhancing foreground regions. Besides, Table V shows the comparison of performance indices, we can see that the SE-MGMM outperforms comparative approaches due to the largest value of KP and $F1$-$score$, the smallest value of OE.

Fig. 12 shows the sixth group of experimental results. The group of bitemporal images is simpler than other testing data since image content only involves water and land. As can be seen from Fig. 12(a) and (b), the pair of bitemporal images provide clear change information in Fig. 12(a)–(c). Although changed regions are clear, the background includes more falsely changed regions caused by noise. Fig. 12(e)–(i), and (k) shows poor results since these methods are sensitive to illumination change and noise. Among them, Fig. 12(i) contains many falsely changed regions, i.e., blue regions, which demonstrates that the CDFFCM is not helpful for this testing data. Fig. 12(j) and (l) shows a better visual effect on really changed regions, where SE-MGMM provides higher values of KP and $F1$-$score$, smaller value of OE than comparative approaches in Table VI.

Tables I, II, V, and VI show that SE-MGMM clearly outperforms the comparative methods, while Table IV shows that they have similar performance. One of the most important reasons is that these groups of testing data including the first, second, third, fifth, and sixth have complex backgrounds, but the fourth group of testing data has simple background. Since the purpose of salience enhancement is to suppress image background and highlight targets, salience enhancement can effectively improve the quality of difference image obtained by bitemporal images with complex background. Consequently, SE-MGMM shows clear advantages than comparative methods for images with complex background as shown in Tables I, II, III, V, and VI.

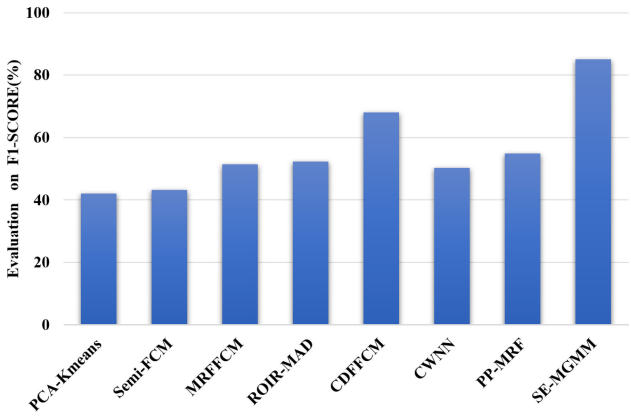

Fig. 13. Performance comparison of different approaches on average values of $F1\text{-}score$.

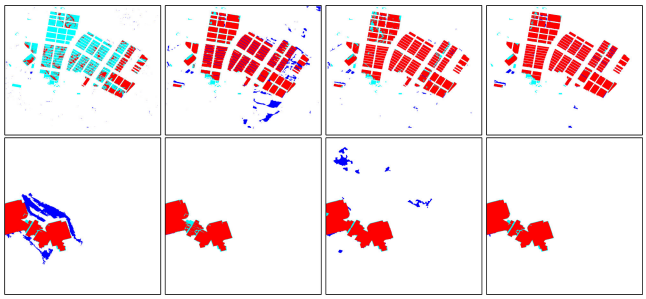

Fig. 14. Comparison of ablation experiments. (a) GMM and postprocessing, (b) SE-GMM, (c) MGMM, and (d) SE-MGMM. Note that the red color denotes truly changed regions, the blue color denotes falsely detected regions, and the cyan color denotes truly missed regions. The changes consist of building changes and construction growth.

Besides, the fourth group of testing data contains richer change information such as farmland, roads and buildings, than other groups of testing data. More changed information easily leads to a difference image with simpler background information. Therefore, SE-MGMM shows slight advantages than comparative methods for images with simple background as shown in Table IV.

D. Discussion

Through the comparison and analysis of our experimental results, the proposed method is effective for change detection on bitemporal remote sensing images. Fig. 13 shows a line chart of change detection results from bitemporal remote sensing images on the average value of $F1\text{-}score$. Obviously, the SE-MGMM provides the highest average value, which shows the SE-MGMM achieves better change detection results and is more robust than comparative approaches.

We verified the effectiveness of different contributions of the proposed SE-MGMM on the first two bitemporal images, by presenting four ablation experiments about GMM, GMM with salient information (SE-GMM), GMM with multi-information fusion (MGMM), and GMM with salient information and multi-information fusion (SE-MGMM). In Fig. 14, the first group of rows corresponds to the change detection results on the first testing data and the second group of rows corresponds to the change detection results on the second testing data. Similarly, test 1 and test 2 in Table VII correspond to the results of the first testing data and the second testing data, respectively. In order to analyze the performance of the proposed method better, all ablation experiments employ the same postprocessing strategy, and four indices are used to evaluate different contributions. From Fig. 14 and Table VII, we can see that SE model is valid for change detection tasks by comparing GMM to SE-GMM and comparing MGMM to SE-MGMM, we can also draw a clear conclusion that multi-information fusion is very useful for improving change detection results by comparing GMM to MGMM.

Beyond that, we further evaluated the proposed method for different bitemporal images under appropriate parameter settings. We use an adaptive postprocessing method described in Section III-C. Therefore the SE-MGMM only involves two required parameters, where C is the number of Gaussian component used for GMM, s is the scale parameter used for multi-information fusion. To test the influence of parameters on the performance of SE-MGMM, we set $C = 4, 5, 6$, $s = 2, 3, 4$, and employ $F1\text{-}score$ to evaluate the experimental results. Similarly, In Tables VIII–IX, test 1 corresponds to the results of the first group of rows in Figs. 15 and 16, and test 2 corresponds to the results of the second group of rows in Figs. 15 and 16. It can be seen from Figs. 15 and 16 and Tables VIII–IX, the proposed

TABLE VII
QUANTITATIVE EVALUATION RESULTS FOR ABLATION EXPERIMENTS, THE BEST VALUES ARE IN BOLD

Test		Evaluation indices			
		OE	CA	KP	$F1\text{-}score$
1	GMM	0.1134	0.8866	0.4024	0.4459
	SE-GMM	0.0455	0.9545	0.8350	0.8622
	MGMM	0.0240	0.9760	0.9072	0.9214
	SE-MGMM	**0.0180**	**0.9820**	**0.9319**	**0.9426**
2	GMN	0.0321	0.9679	0.7732	0.7901
	SE-GMM	0.0240	0.9760	0.9072	0.9214
	MGMM	0.0455	0.9545	0.8350	0.8622
	SE-MGMM	**0.0049**	**0.9951**	**0.9581**	**0.9607**

TABLE VIII
QUANTITATIVE EVALUATION RESULTS ON $F1\text{-}score$ USING DIFFERENT VALUES OF C

Test	$C = 4$	$C = 5$	$C = 6$
1	0.9328	0.9426	0.9277
2	0.9456	0.9607	0.9596

TABLE IX
QUANTITATIVE EVALUATION RESULTS ON $F1\text{-}score$ USING DIFFERENT VALUES OF s

Test	$s = 2$	$s = 3$	$s = 4$
1	0.9426	0.9237	0.9262
2	0.9607	0.9513	0.9594

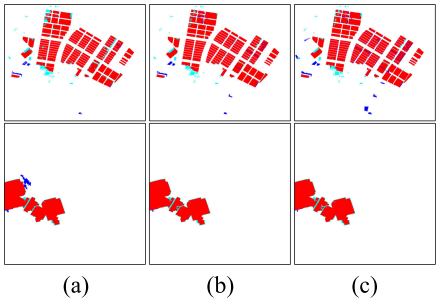

Fig. 15. Comparison of change detection results using different values of C. (a) $C = 4$, (b) $C = 5$, and (c) $C = 6$. Note that the red color denotes truly changed regions, the blue color denotes falsely detected regions, and the cyan color denotes truly missed regions. The changes consist of building changes and construction growth.

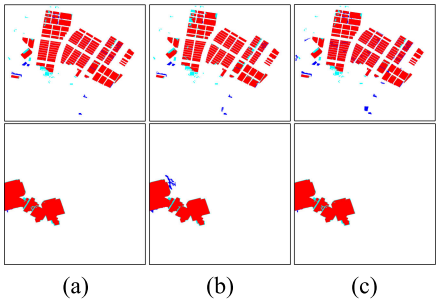

Fig. 16. Comparison of change detection results using different values of s. (a) $s = 2$, (b) $s = 3$, and (c) $s = 4$. Note that the red color denotes truly changed regions, the blue color denotes falsely detected regions, and the cyan color denotes truly missed regions. The changes consist of building changes and construction growth.

TABLE X
COMPARISON OF RUNNING TIME (SECONDS) USING DIFFERENT METHODS ON ALL TESTING DATA, THE BEST VALUES ARE IN BOLD

Method	1	2	3	4	5	6
PCA-Kmeans [11]	637.99	38.52	19.22	17.49	12.83	4.38
Semi-FCM [12]	231.80	15.93	10.78	8.40	5.91	5.28
MRFFCM [20]	257.41	**13.79**	**5.48**	**3.82**	**3.30**	**3.23**
IRO-MAD [19]	269.62	17.34	7.97	6.99	5.83	5.16
CDFFCM [14]	**221.19**	13.51	7.27	5.58	5.85	4.97
CWNN [56]	-	75.43	55.56	61.71	96.76	79.12
PP-MRF [22]	249.67	23.19	10.41	9.85	9.34	8.93
SE-MGMM	404.13	39.64	16.76	16.77	9.89	4.15

approach is insensitive to parameters, which further verifies the robustness of our proposed method.

Finally, Table X illustrates the computational cost of comparative methods and our proposed method on testing images with different sizes. In Table X, the CDFFCM is much faster than other methods for the first testing data, and the MRFFCM is much faster than other methods for other five groups of testing data. The proposed SE-MGMM is time consuming since the covariance is computed in GMM. But this drawback is compensated by its better performance on $F1\text{-}score$. Note that, "1"–"6" in Table X represent the corresponding testing data.

V. CONCLUSION

In this work, we have studied the popular change detection approaches and analyzed their advantages and disadvantages. We have proposed an unsupervised change detection using multiscale and multiresolution SE-MGMM for bitemporal remote sensing images. The proposed SE-MGMM can effectively achieve change detection result and makes two useful contributions. The first is that the SE-MGMM is insensitive to illumination change due to the employment of saliency difference information. The second is that it can make full use of richer feature information in bitemporal images due to the employment of GMM-SMFM. The proposed SE-MGMM is tested on six groups of remote sensing images, and experimental results demonstrate that the proposed SE-MGMM is superior to state-of-the-art change detection methods since it provides the best results. In future works, we will explore more robust and fast algorithms for change detection to solve this problem.

REFERENCES

[1] X. Huang, D. Wen, J. Li, and R. Qin, "Multi-level monitoring of subtle urban changes for the megacities of China using high-resolution multi-view satellite imagery," *Remote Sens. Environ.*, vol. 196, pp. 56–75, Jul. 2017.

[2] P. Fu and Q. Weng, "A time series analysis of urbanization induced land use and land cover change and its impact on land surface temperature with Landsat imagery," *Remote Sens. Environ.*, vol. 175, pp. 205–214, Mar. 2016.

[3] J. L. Gil-Yepes, L. A. Ruiz, and J. A. Recio, "Description and validation of a new set of object-based temporal geostatistical features for land-use/land-cover change detection," *J. Photogramm. Remote Sens.*, vol. 121, pp. 77–91, Nov. 2016.

[4] K. Islam, M. Jashimuddin, B. Nath, and T. K. Nath, "Land use classification and change detection by using multi-temporal remotely sensed imagery: The case of Chunati wildlife sanctuary, Bangladesh," *Egypt. J. Remote Sens. Space Sci.*, vol. 21, no. 1, pp. 37–47, Apr. 2018.

[5] X. Zhan *et al.*, "Monitoring surface type changes with S-NPP/JPSS VIIRS observations," in *Proc. IEEE Geosci. Remote Sens. Symp.*, Jul. 2017, pp. 1288–1291.

[6] N. Mohamed and B. Mobarak, "Change detection techniques using optical remote sensing: A survey," *Amer. Scientific Res. J. Eng. Technol. Sci.*, vol. 17, no. 1, pp. 42–51, Nov. 2016.

[7] S. Aminikhanghahi and D. J. Cook, "A survey of methods for time series change point detection," *Knowl. Inf. Syst.*, vol. 51, no. 2, pp. 339–367, Mar. 2017.

[8] N. Khabou, I. B. Rodriguez, G. Gharbi, and M. Jmaiel, "A threshold-based context change detection in pervasive environments: Application to a smart campus," *Procedia Comput. Sci.*, vol. 32, no. 10, pp. 461–468, Oct. 2014.

[9] Z. Lv, W. Shi, X. Zhang, and J. A. Benediktsson, "Landslide inventory mapping from bitemporal high-resolution remote sensing images using change detection and multiscale segmentation," *IEEE J. Sel. Topics Appl. Earth Observ. Remote Sens.*, vol. 11, no. 5, pp. 1520–1532, May 2018.

[10] D. H. Tran, "Automated change detection and reactive clustering in multivariate streaming data," in *Proc. IEEE Int. Conf. Comput. Commun. Technol.*, Mar. 2019, pp. 1–6.

[11] T. Celik, "Unsupervised change detection in satellite images using principal component analysis and k-means clustering," *IEEE Geosci. Remote Sens. Lett.*, vol. 6, no. 4, pp. 772–776, Mar. 2009.

[12] P. Shao, W. Shi, P. He, M. Hao, and X. Zhang, "Novel approach to unsupervised change detection based on a robust semi-supervised FCM clustering algorithm," *Remote Sens.*, vol. 8, no. 3, Mar. 2016, Art. no. 264.

[13] M. Hao, Z. Hua, Z. Li, and B. Chen, "Unsupervised change detection using a novel fuzzy c-means clustering simultaneously incorporating local and global information," *Multimed. Tools. Appl.*, vol. 76, no. 19, pp. 20081–20098, Jan. 2017.

[14] T. Lei, D. Xue, Z. Lv, Y. Zhang, and A. K. Nandi, "Unsupervised change detection using fast fuzzy clustering for landslide mapping from very high-resolution images," *Remote Sens.*, vol. 10, no. 9, Aug. 2018, Art. no. 1381.

[15] G. Yang, H. Li, W. Wang, W. Yang, and W. J. Emery, "Unsupervised change detection based on a unified framework for weighted collaborative representation with RDDL and fuzzy clustering," *IEEE Trans. Geosci. Remote Sens.*, vol. 57, no. 11, pp. 8890–8903, Nov. 2019.

[16] Z. Lv, T. Liu, Y. Wan, J. A. Benediktsson, and X. Zhang, "Post-processing approach for refining raw land cover change detection of very high-resolution remote sensing images," *Remote Sens.*, vol. 10, no. 3, Mar. 2018, Art. no. 472.

[17] M. Zanetti, B. Francesca, and B. Lorenzo, "Rayleigh-rice mixture parameter estimation via EM algorithm for change detection in multispectral images," *IEEE Trans. Image Process.*, vol. 24, no. 12, pp. 5004–5016, Aug. 2015.

[18] M. J. Canty and A. A. Nielsen, "Automatic radiometric normalization of multitemporal satellite imagery with the iteratively re-weighted MAD transformation," *Remote Sens. Environ.*, vol. 112, no. 3, pp. 1025–1036, Mar. 2008.

[19] Q. Xu, Z. Liu, F. Li, M. Yang, and H. Ren, "The regularized iteratively reweighted object-based MAD method for change detection in bi-temporal, multispectral data," in *Proc. Int. Symp. Hyperspectral Remote Sens. Appl. Environ. Monit. Saf. Testing Technol.*, Beijing, China, Oct. 2019, Art. no. 10156.

[20] M. Gong, L. Su, M. Jia, and W. Chen, "Fuzzy clustering with a modified MRF energy function for change detection in synthetic aperture radar images," *IEEE Trans. Fuzzy Syst.*, vol. 22, no. 1, pp. 98–109, Feb. 2014.

[21] H. Yu, W. Yang, G. Hua, H. Ru, and P. Huang, "Change detection using high resolution remote sensing images based on active learning and Markov random fields," *Remote Sens.*, vol. 9, no. 12, Nov. 2017, Art. no. 101560P.

[22] R. Touati, M. Max, and D. Mohamed, "Multimodal change detection in remote sensing images using an unsupervised pixel pairwise-based Markov random field model," *IEEE Trans. Image Process.*, vol. 29, pp. 757–767, Aug. 2019.

[23] Y. Yang, X. Cong, K. Long, Y. Luo, X. Wei, and Q. Wan, "MRF model-based joint interrupted SAR imaging and coherent change detection via variational Bayesian inference," *Signal Process.*, vol. 151, pp. 144–154, Oct. 2018.

[24] Z. Li, W. Shi, S. Myint, P. Lu, and Q. Wang, "Semi-automated landslide inventory mapping from bitemporal aerial photographs using change detection and level set method," *Remote Sens. Environ.*, vol. 175, pp. 215–230, Mar. 2016.

[25] X. Zhang, W. Shi, M. HaoS. Pan, and X. Lyu, "Level set incorporated with an improved MRF model for unsupervised change detection for satellite images," *Eur. J. Remote Sens.*, vol. 50, pp. 202–210, Mar. 2017.

[26] J. Liu, M. Gong, K. Qin, and P. Zhang, "A deep convolutional coupling network for change detection based on heterogeneous optical and radar images," *IEEE Trans. Neural Netw. Learn. Syst.*, vol. 29, no. 3, pp. 545–559, Dec. 2018.

[27] Q. Wang, Z. Yuan, Q. Du, and X. Li, "GETNET: A. general end-to-end 2-D CNN framework for hyperspectral image change detection," *IEEE Trans. Geosci. Remote Sens.*, vol. 57, no. 1, pp. 3–13, Jan. 2019.

[28] T. Lei, Y. Zhang, Z. Lv, S. Li, S. Liu, and A. K. Nandi, "Landslide inventory mapping from bitemporal images using deep convolutional neural networks," *IEEE Geosc. Remote Sens. Lett.*, vol. 16, no. 6, pp. 982–986, Jun. 2019.

[29] R. C. Daudt, B. Le Saux, A. Boulch, and Y. Gousseau, "Multitask learning for large-scale semantic change detection," *Comput. Vis. Image Understanding*, vol. 187, no. 10, Oct. 2019, Art. no. 102783.

[30] D. Peng, Y. Zhang, and H. Guan, "End-to-end change detection for high resolution satellite images using improved UNet," *Remote Sens.*, vol. 11, no. 11, Jun. 2019, Art. no. 1382.

[31] L. Khelifi and M. Mignotte, "Deep learning for change detection in remote sensing images: Comprehensive review and meta-analysis," *IEEE Access*, vol. 8, no. 6, pp. 126385–126400, 2020.

[32] W. Shi, M. Zhang, R. Zhang, S. Chen, and Z. Zhan, "Change detection based on artificial intelligence: State-of-the-art and challenges,"*Remote Sens*, vol. 12, no. 10, May 2019, Art. no. 1688.

[33] W. Shi *et al.*, "Landslide recognition by deep convolutional neural network and change detection," *IEEE Trans. Geosci. Remote Sens*, to be published, doi: 10.1109/TGRS.2020.3015826.

[34] A.Anju and J. Anitha, "Change detection techniques for remote sensing applications: A survey," *Earth Sci. Inform.*, vol. 12, no. 2, pp. 143–160, Mar. 2019.

[35] M. Gong, Z. Zhou, and J. Ma, "Change detection in synthetic aperture radar images based on image fusion and fuzzy clustering," *IEEE Trans. Image Process.*, vol. 21, no. 4, pp. 2141–2151, Apr. 2012.

[36] Z. Li, W. Shi, H. Zhang, and M. Hao, "Change detection based on Gabor wavelet features for very high-resolution remote sensing images," *IEEE Geosci. Remote Sens.*, vol. 14, no. 5, pp. 783–787, May 2017.

[37] X. Zhang, T. Wang, J. Qi, H. Lu, and G. Wang, "Progressive attention guided recurrent network for salient object detection," in *Proc. IEEE Conf. Comput Vis. Pattern Recognit.*, 2018, pp. 714–722.

[38] X. Hu, L. Zhu, J. Qin, and H. Lu, "Recurrently aggregating deep features for salient object detection," in *Proc. 32nd AAAI Conf. Artif. Intell.*, Apr. 2018, pp. 6943–6950.

[39] J. Zhao, Y. Cao, D. Fan, M. Cheng, X. Li, and L. Zhang, "Contrast prior and fluid pyramid integration for RGBD salient object detection," in *Proc. IEEE Conf. Comput. Vis. Pattern Recognit.*, Long Beach, CA, USA, 2019, pp. 3922–3931.

[40] Z. Zhu, H. Yin, Y. Chai, Y. Li and G. Qi, "A novel multi-modality image fusion method based on image decomposition and sparse representation," *Inf. Sci.*, vol. 432, pp. 516–529, Mar. 2018.

[41] R. Dian, S. Li, L. Fang, and W. Qi, "Multispectral and hyperspectral image fusion with spatial-spectral sparse representation," *Inf. Fusion*, vol. 49, pp. 262–270, Sep. 2019.

[42] J. Ma *et al.*, "Infrared and visible image fusion via detail preserving adversarial learning," *Inf. Fusion*, vol. 54, pp. 85–98, Feb. 2020.

[43] J. Ma, Y. Ma, and C. Li, "Infrared and visible image fusion methods and applications: A survey," *Inf. Fusion*, vol. 45, pp. 153–178, Jan. 2019.

[44] F. Vollnhals, J. N. Audinot, T. Wirtz, M. M. Bonin, and I. Fourquaux, "Correlative microscopy combining secondary ion mass spectrometry and electron microscopy: Comparison of intensity-hue-saturation and Laplacian pyramid methods for image fusion," *Anal. Chem.*, vol. 89, no. 20, pp. 10702–10710, Sep. 2017.

[45] G. Ravikanth, K. V. N. Sunitha, and B. E. Reddy, "Intensity-hue-saturation renovation and local deviation methods for satellite image fusion metric assessment," *Int. J. Appl. Pattern Recognit.*, vol. 5, no. 4, pp. 280–292, Jan. 2018.

[46] C. Lu, J. Feng, Y. Chen, W. Liu, Z. Lin and S. Yan, "Tensor robust principal component analysis with a new tensor nuclear norm," *IEEE Trans. Pattern Analysis. Mach. Intell.*, vol. 42, no. 4, pp. 925–938, Apr. 2020.

[47] Y. Ait-Sahalia, and D. Xiu, "Principal component analysis of high-frequency data," *J. Statist. Assoc.*, vol. 114, no. 525, pp. 287–303, Aug. 2019.

[48] C. Shi, Q. Miao, and P. Xu, "A novel algorithm of remote sensing image fusion based on Shearlets and PCNN," *Neurocomputing*, vol. 117, pp. 47–53, Oct. 2013.

[49] U. Kumar, C. Milesi, and R. R. Nemani, "Multi-sensor multi-resolution image fusion for improved vegetation and urban area classification," *Remote Sens. Spat. Inf. Sci.*, vol. 40, no. 7, pp. 51–58, Jun. 2015.

[50] L. Zhou, Z. Yang, Q. Yuan, Z. Zhou, and D. Hu, "Salient region detection via integrating diffusion-based compactness and local contrast," *IEEE Trans. Image Process.*, vol. 24, no. 11, pp. 3308–3320, Nov. 2015.

[51] J. Han, G. Cheng, Z. Li, and D. Zhang, "A unified metric learning-based framework for co-saliency detection," *IEEE Trans. Circuits Syst. Video Technol.*, vol. 28, no. 10, pp. 2473–2483, Oct. 2018.

[52] L. Zhang, A. Li, Z. Zhang, and K. Yang, "Global and local saliency analysis for the extraction of residential areas in high-spatial-resolution remote sensing image," *IEEE Trans. Geosci. Remote Sens.*, vol. 54, no. 7, pp. 3750–3763, Jul. 2016.

[53] N. Liu and J. Han, "A deep spatial contextual long-term recurrent convolutional network for saliency detection," *IEEE Trans. Image Process.*, vol. 27, no. 7, pp. 3264–3274, Jul. 2018.

[54] T. Lei, X. Jia, T. Liu, S. Liu, H. Meng, and A. K. Nandi, "Adaptive morphological reconstruction for seeded image segmentation," *IEEE Trans. Image Process.*, vol. 28, no. 11, pp. 5510–5523, Nov. 2019.

[55] T. Lei, X. Jia, Y. Zhang, S. Liu, H. Meng, and A. K. Nandi, "Superpixel-based fast fuzzy c-means clustering algorithms for color image segmentation," *IEEE Trans. Fuzzy Syst.*, vol. 27, no. 9, pp. 1753–1766, Sep. 2019.

[56] F. Gao, X. Wang, Y. Gao, J. Dong, and S. Wang, "Sea ice change detection in SAR images based on convolutional-wavelet neural networks," *IEEE Geosci. Remote Sens. Lett.*, vol. 16, no. 8, pp. 1240–1244, Feb. 2019.

[57] D. Peng, L. Bruzzone, Y. Zhang, H. Guan, H. Ding, and X. Huang, "SemiCDNet: A semisupervised convolutional neural network for change detection in high resolution remote-sensing images," *IEEE Trans. Geosci. Remote Sens.*, vol. 6, pp. 1–6, Aug. 2020.

[58] H. Chen and Z. Shi, "A spatial-temporal attention-based method and a new dataset for remote sensing image change detection," *Remote Sens.*, vol. 12, no. 10, Apr. 2020, Art. no. 1662.

[59] B. Héloïse and L. Antoinet, "Lamboisenet," 2020. [Online]. Available: https://github.com/hbaudhuin/LamboiseNet

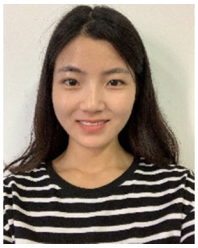

Dinghua Xue received the M.S. degree in control science and engineering from the Shaanxi University of Science and Technology, Xi'an, China, in 2019. She is currently working toward the Ph.D. degree in light chemical industrial process systems and engineering with the School of Electrical and Control Engineering, Shaanxi University of Science and Technology, Xi'an, China.

Her current research interests include image processing and pattern recognition.

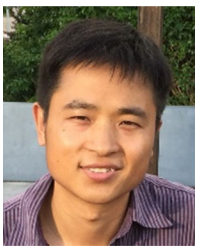

Tao Lei (Senior Member, IEEE) received the Ph.D. degree in information and communication engineering from Northwestern Polytechnical University, Xi'an, China, in 2011.

From 2012 to 2014, he was a Postdoctoral Research Fellow with the School of Electronics and Information, Northwestern Polytechnical University, Xi'an, China. From 2015 to 2016, he was a Visiting Scholar with the Quantum Computation and Intelligent Systems group, University of Technology Sydney, Sydney, Australia. He has authored and coauthored 80+ research papers including IEEE TIP, TFS, TGRS, TGRSL, ICASSP, ICIP, and FG. He is currently a Professor with the School of Electronic Information and Artificial Intelligence, Shaanxi University of Science and Technology, Xi'an, China. His current research interests include image processing, pattern recognition, and machine learning.

Xiaohong Jia received the M.S. degree in signal and information processing from Lanzhou Jiaotong University, Lanzhou, China, in 2017. He is currently working toward the Ph.D. degree in light chemical industrial process systems and engineering with the School of Electronical and Control Engineering, Shaanxi University of Science and Technology, Xi'an, China.

His current research interests include image processing and pattern recognition.

Xingwu Wang received the bachelor's degree in information security from Xidian University, Xi'an, China, in 2019. He is working toward the M.S. degree in software engineering with the School of Electronic Information and Artificial Intelligence, Shaanxi University of Science and Technology, Xi'an, China.

His current research interests include image processing and pattern recognition.

Tao Chen (Member, IEEE) received the Ph.D. degree in photogrammetry and remote sensing from Wuhan University, Wuhan, China, in 2008.

From 2015 to 2016, he was a Visiting Scholar with the University of New South Wales, Sydney, Australia. He has authored or coauthored more than 40 scientific papers including *IEEE JSTARS*, *Remote Sensing*, *Environmental Earth Sciences*, and *Environmental Science and Pollution Research*. He is currently an Associate Professor with the Institute of Geophysics and Geomatics, China University of Geosciences, Wuhan, China. His research interests include image processing, machine learning, and geological remote sensing.

Asoke K. Nandi (Fellow, IEEE) received the Ph.D. degree in light chemical industrial process systems and engineering from the University of Cambridge (Trinity College), Cambridge, U.K., in 1979.

He held academic positions in several universities, including University of Oxford, Oxford, U.K., Imperial College London, London, U.K., University of Strathclyde, Glasgow, U.K., and University of Liverpool, Liverpool, U.K., as well as Finland Distinguished Professorship in Jyvaskyla, Finland. In 2013, he moved to Brunel University London, Uxbridge, U.K., to become the Chair and Head of Electronic and Computer Engineering. He is a Distinguished Visiting Professor with Xi'an Jiaotong University, Shanghai, China and an Adjunct Professor with the University of Calgary, Calgary, AB Canada. He was an IEEE EMBS Distinguished Lecturer during 2018–2019. In 1983, he co-discovered the three fundamental particles known as W^+, W^-, and Z^0 (by the UA1 team at CERN), providing the evidence for the unification of the electromagnetic and weak forces, for which the Nobel Committee for Physics in 1984 awarded the prize to his two team leaders for their decisive contributions. He has made many fundamental theoretical and algorithmic contributions to many aspects of signal processing and machine learning. He has much expertise in "Big and Heterogeneous Data", dealing with modeling, classification, estimation, and prediction. He has authored over 600 technical publications, including 250 journal papers as well as five books, entitled *Condition Monitoring with Vibration Signals: Compressive Sampling and Learning Algorithms for Rotating Machines* (Hoboken, NJ: Wiley, 2020), *Automatic Modulation Classification: Principles, Algorithms and Applications* (Hoboken, NJ: Wiley, 2015), *Integrative Cluster Analysis in Bioinformatics* (Hoboken, NJ: Wiley, 2015), *Blind Estimation Using Higher-Order Statistics* (New York, NY: Springer, 1999), and *Automatic Modulation Recognition of Communications Signals* (New York, NY: Springer, 1996). The H-index of his publications is 80 (Google Scholar) and his ERDOS number is 2. His current research interests include signal processing and machine learning, with applications to communications, image segmentations, biomedical data, etc.

Prof. Nandi is a Fellow of the Royal Academy of Engineering, U.K. as well as a Fellow of seven other institutions, including the IEEE and the IET. Among the many awards he received are the Institute of Electrical and Electronics Engineers, USA, Heinrich Hertz Award, in 2012, the Glory of Bengal Award for his outstanding achievements in scientific research, in 2010, the Water Arbitration Prize of the Institution of Mechanical Engineers, U.K., in 1999, and the Mountbatten Premium, Division Award of the Electronics and Communications Division, of the Institution of Electrical Engineers, U.K., in 1998. He was an IEEE EMBS Distinguished Lecturer during 2018–2019.